Journal of Materials Chemistry A

ROYAL SOCIETY OF CHEMISTRY

PAPER

Cite this: J. Mater. Chem. A, 2023, 11, 965

Rationally designed titanium-based metal–organic frameworks for visible-light activated chemiresistive sensing†

Hui-Zi Li,‡[a] Yu Pan,‡[a] Qiaohong Li,[a] Qipu Lin,[a] Duoyu Lin,[b] Fei Wang,*[a] Gang Xu*[a] and Jian Zhang*[a]

Received 15th November 2022
Accepted 5th December 2022

DOI: 10.1039/d2ta08921a

rsc.li/materials-a

Simultaneously realizing high sensitivity and high selectivity at room temperature is still a big challenge for designing chemiresistive gas sensing materials. In this work, the first visible-light active MOF sensing material was rationally designed and prepared to meet this challenge. Different from the reported MOFs, FIR-120 combines a high stability, permanent porosity and visible light active titanium-phenol functional motif in one structure through an interpenetrating structure strategy. These features endow FIR-120 with unique photo-physic/chemistry properties that enable the highest sensitivity, lowest experimental limit-of-detection (LOD) and excellent selectivity to NO_2 among all reported MOFs and MOF composite materials at room temperature. Moreover, the structure–sensing relationship is studied through experiments and theoretical calculations. This work provides guidance for the design and synthesis of high-performance visible-light active MOFs and leads to a new type of gas sensing material.

Introduction

The precise detection of gaseous species is critical to environmental protection, industrial process control, agricultural production, and public health & safety. Compared with other gas detection techniques, chemiresistive sensors are superior in terms of low cost, easy fabrication, not needing a professional operator, and real-time online monitoring.[1–11] However, the predominant sensing materials, metal oxides, are still limited by high working temperature, low sensitivity at room temperature and selectivity.[1] Researchers have found that the free charges generated by light irradiation can effectively enhance the sensitivity of metal oxides at room temperature.[12] However, the intrinsically wide bandgaps of metal oxides make them excited only by ultraviolet light which not only requires high cost equipment but also generates strong interfering substances such as ozone, due to its high energy.[13] Moreover, it is still a big challenge for light-assistant sensing materials to realize highly selective sensing. To develop a new type of room temperature sensing material that can be activated by visible light and possess both high sensitivity and selectivity is extremely desired.

Metal–organic frameworks (MOFs)[14] are a new generation of gas sensing materials that are able to work at room temperature.[15–18] Their highly adjustable porous structures provided excellent sensing selectivity to target analytes.[19] However, the reported MOFs still have low sensitivity at room temperature, which hinders their further application.[19–25] Titanium-based metal–organic frameworks (Ti-MOFs) are known as one kind of very important photoactive semiconductor material and have attracted a lot of research interest in photocatalysis and other fields.[26–38] Thus, it is expected to obtain high gas sensing sensitivity by utilizing the photoactivity of Ti-MOFs. Nevertheless, the low electrical conductivity should be the main challenge that hindered the use of such Ti-MOFs for resistive sensing. In addition, it is quite difficult to obtain highly crystalline Ti-MOFs due to the high reactivity of Ti^{4+} ions. Stable Ti-MOFs can be constructed by bridging Ti atoms with carboxylic acid ligands, but most of them show weak visible light absorption and wide band gaps in the range of 2.5–3.0 eV.[39] To solve this problem, phenolic ligands were introduced to form a titanium-phenol functional motif which enables metal charge transfer (LMCT) to improve visible light absorption.[40–46] Two reported Ti-MOFs, NTU-9 (ref. 40) and MIL-167 (ref. 42) synthesized by this strategy exhibit deep red color and strong absorption in a wide visible region with lower band gaps (1.7–1.8 eV). Therefore, phenolic ligand based Ti-MOFs are

[a]State Key Laboratory of Structural Chemistry, Fujian Institute of Research on the Structure of Matter, Chinese Academy of Sciences, Fuzhou, Fujian 350002, P. R. China. E-mail: wangfei04@fjirsm.ac.cn; gxu@fjirsm.ac.cn; zhj@fjirsm.ac.cn

[b]MOE Key Laboratory of Bioinorganic and Synthetic Chemistry, School of Chemistry, Sun Yat-Sen University, Guangzhou 510275, P. R. China

† Electronic supplementary information (ESI) available: The synthesis, IR and PXRD data, stability tests, sensing property test and theoretical calculations. The X-ray crystallographic coordinates for structures reported in this article have been deposited at the Cambridge Crystallographic Data Centre (CCDC) under deposition numbers CCDC 2034734 (FIR-120). For ESI and crystallographic data in CIF or other electronic format see DOI: https://doi.org/10.1039/d2ta08921a

‡ These authors contributed equally to this paper.

considered favorable candidates to realize visible light activated sensing materials with both high sensitivity and selectivity. Unfortunately, the poor chemical stability of NTU-9 and lack of porosity of MIL-167 limit their application in chemiresistive sensing. Therefore, it is a very challenging task to synthesize visible light active Ti-MOFs with both permanent porosity and excellent chemical stability as efficient chemiresistive sensors.

The formation of interpenetrating structures is an effective means to stabilize the porous structures of MOFs and the employment of long organic ligands is a common strategy to realize this aim.[47] Based on these considerations, elongated phenolic ligand, 4,4′-dihydroxy-[1,1′-biphenyl]-3,3′-dicarboxylic acid (H_4dobpdc), was rationally selected to synthesize single crystal Ti-MOF (denoted as FIR-120, FIR = Fujian Institute Research), which exhibits a 6-fold interpenetrated srs framework with permanent porosity and excellent thermal and chemical stability. FIR-120 exhibits strong visible light absorption ($E_g = 1.87$ eV) owing to effective LMCT, which significantly enhances its sensing performances compared with those in the dark. As a NO_2 sensing material, FIR-120 achieves the highest sensitivity, lowest experimental limit-of-detection (LOD) and excellent selectivity among all reported MOFs and MOF composite materials at room temperature. In addition, the structure–activity relationship based on the crystal structure is established through experiments and theoretical calculations. It is worth noting that this is the first time that visible light active MOF chemiresistive sensing materials have been reported.

In this work, red prism-like single crystals (Fig. 1a) were obtained by heating a mixture of $Ti(O^iPr)_4$ and H_4dobpdc in 1,4-dioxane/acetic acid at 160 °C for 7 days (see the ESI for details†). Single crystal X-ray diffraction analysis reveals that FIR-120 crystallized in a tetragonal space group $I4_1$ (Table S1†). In FIR-120, each Ti atom is octahedrally coordinated with six oxygen atoms from phenol hydroxide and carboxylate groups (Fig. 1d), quite similar to the Ti center in cation·[Ti(SA)$_3$] compounds (H_2SA = salicylic acid)[48] as well as in NTU-9 and MIL-167. Differently, the octahedral Ti center was connected by short dobdc (2,5-dioxido-1,4-benzenedicarboxylate) ligands to form a 3D three-dimensional (3D) framework in MIL-167 with 2-fold interpenetrated srs topology.[49] A large amount of counterions in the pores led to the framework non-porosity. In FIR-120, the employment of longer dobpdc ligands (Ti⋯Ti distance from 12.423 to 12.562 Å) led to the formation of a 3D framework with 6-fold (3 + 3) interpenetrated srs topology (Fig. 1b and c). Similar to NTU-9, parts of the carboxylates retained protons as they were synthesized under acidic conditions, giving the neutral framework with the formula $Ti_8(Hdobpdc)_8(H_2dobpdc)_4$, which has cavities of about 4–6 Å free diameter (Fig. S3a†) calculated by Poreblazer.[50] All uncoordinated –OH from the carboxylate groups point to the 1-D channels. After removing guests in the channels, the solvent-accessible void in the structure of FIR-120 was calculated to be about 55.3% using PLATON.[51]

The powder XRD (PXRD) pattern of as synthesized FIR-120 shows that most of the main peaks are well consistent with the simulated pattern, which confirmed the phase purity of the material (Fig. S1†). The highly interpenetrated framework

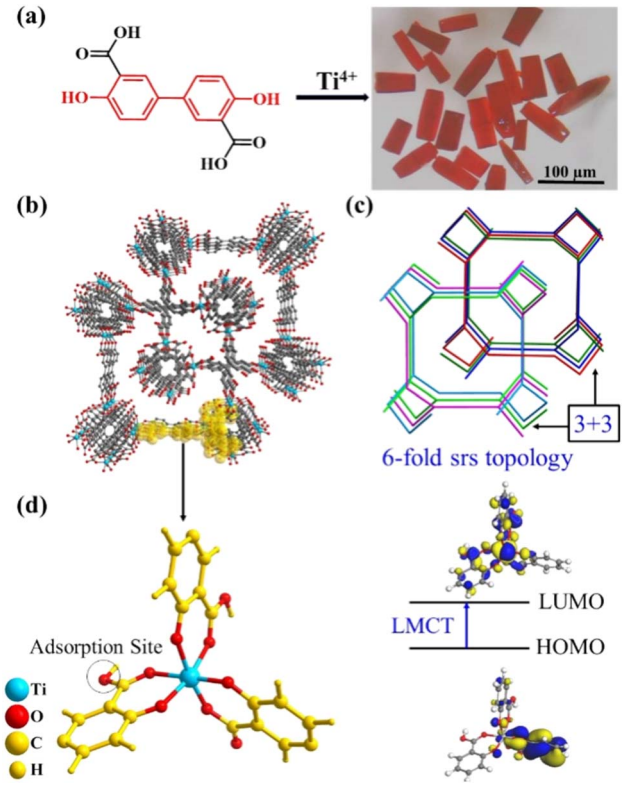

Fig. 1 (a) Synthetic route and optical microscope image of single crystalline FIR-120. (b) View of the 3D framework along the *c*-axis. (c) View of the 6-fold interpenetrated srs topology. (d) The calculated HOMO and LUMO based TiL_3 unit. Uncoordinated –OH of the carboxylate group as potential NO_2 adsorption sites.

endows FIR-120 with excellent stability. Powder XRD measurements demonstrate that FIR-120 was stable after soaking in common solvents such as DMF, ethanol, acetonitrile, ethyl acetate (EA) and 1,4-dioxane at room temperature for 24 hours (Fig. 2a). FIR-120 also exhibited good water stability in water for 21 days at room temperature or in boiling water for 1 day (Fig. S2†). The thermogravimetric (TG) results (Fig. 2b) of the as-synthesized samples in an N_2 atmosphere indicated a *ca.* 8% weight loss from 25 to *ca.* 120 °C, which was assigned to the guest molecules such as CH_3CO_2H, 1,4-dioxane and isopropanol, respectively. Then the clear platform extending to 230 °C suggested good thermal stability and porosity of FIR-120. The CO_2 adsorption at 195 K further proved the permanent porosity of FIR-120. The BET surface area of FIR-120 is *ca.* 544 $m^2 g^{-1}$ (Fig. 2c and S3†), which is much higher than that of most metal oxide sensing materials.

UV-vis diffuse reflectance spectroscopy shows that FIR-120 has strong absorption in visible light ranging from 400–800 nm (Fig. 2d). The band gap of FIR-120 is calculated to be 1.87 eV according to the Tauc plot (Fig. S4†), suggesting its semiconductor nature. *I–V* curves of FIR-120 at different temperatures show linear contours, indicating ohmic contact between the sample and the electrode (Fig. S5†). The conductivity of FIR-120 increases with an increase in temperature and this together with the good linear relationship of $\ln \sigma \sim 1000/T$

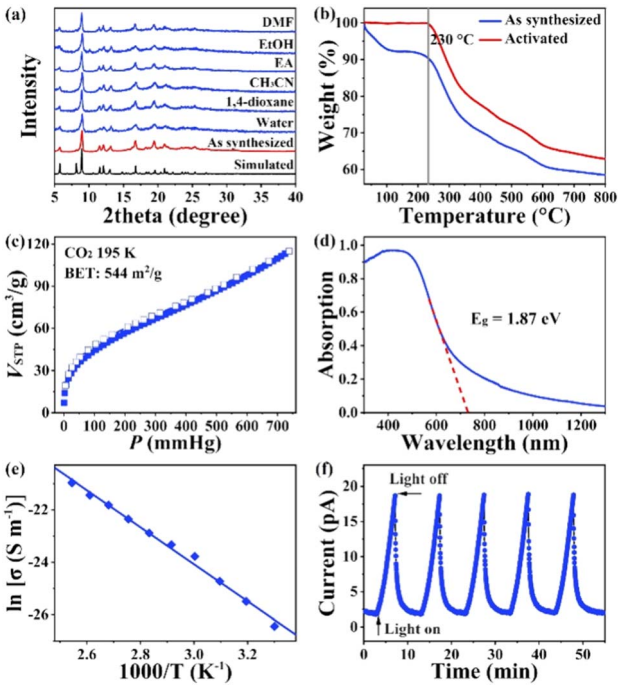

Fig. 2 (a) Powder XRD patterns of FIR-120 treated with different solvents for 24 h. (b) Thermogravimetric (TG) curve of as synthesized and activated FIR-120. (c) CO_2 adsorption–desorption isotherm of FIR-120 at 195 K. (d) UV-vis diffuse reflectance spectra of FIR-120. (e) Fitting of conductivity–temperature data to the Arrhenius equation. (f) Photo-current of FIR-120 under visible light periodic illumination ($\lambda \geq$ 420 nm, 300 W; 15 A, Fig. S6†).

confirms the semiconductor characteristics of FIR-120 (Fig. 2e). The photo-current of FIR-120 can be reversibly modulated by periodic visible light irradiation with little degradation for 5 cycles, indicating its excellent visible light activity (Fig. 2f).

The integration of large amounts of free –OH, excellent stability, permanent porosity and visible light activity of FIR-120 makes it a good candidate for gas sensing. Therefore, the NO_2 gas sensing performance of FIR-120 was studied at room temperature. When exposed to 10 ppm NO_2 under dark conditions, the current intensity of FIR-120 increased and returned to the initial value after purging with dry air (Fig. 3a). However, it takes a long time (30 minutes) to fully recover under dark conditions indicating a slow desorption process (Fig. S7†). Considering that FIR-120 exhibits strong visible light absorption (E_g = 1.87 eV) owing to effective LMCT, visible light was utilized to optimize performance. As shown in Fig. 3a and c, compared with those under dark conditions, recovery time is efficiently shortened and the response to 10 ppm NO_2 is increased by 2 times and reaches 2040% under visible light (Fig. 3b and c). The reversible response and recovery time are 2.48 and 2.60 minutes, respectively (Fig. S8†). What's more, FIR-120 exhibited the dynamic response and recovery curve to a wide concentration range of NO_2 (Fig. 3c) and it showed the highest response among all reported MOFs and MOF composites under visible light (Fig. 3f and Table 1). The experimental limit of detection (LOD) for FIR-120 to NO_2 was 40 ppb which is also the best one among those of all reported MOFs and MOF composites (Fig. 3d and Table 1). Due to the strong interaction between the reported MOF and NO_2, MOF sensing materials usually require high temperature for recovery.[19] Thus, FIR-120 represents the first pure MOF sensing material that shows high sensitivity and can reversibly detect NO_2 at room temperature.

FIR-120 also shows excellent selectivity to NO_2 over other 15 interfering gases (Fig. 3e and S10†). It has 26 times higher response to 10 ppm NO_2 than to 100 ppm SO_2, the strongest inference (Table S2†). The continuous cycling tests of FIR-120 (Fig. 3c) showed that the response coefficient of variation (CV) was only 2.8% in 5 cycles toward 10 ppm NO_2, which suggested its excellent repeatability. The PXRD results after illumination and NO_2 exposure (Fig. S11a†) confirm the good stability of FIR-120. In addition, the retention rate of response values toward 10 ppm NO_2 after storage for 70 days was *ca.* 100%, indicating that the FIR-120 sensor has good long-term stability (Fig. S11b†). In addition, FIR-120 maintains high response values in a wide range of relative humidity (Fig. S12†). These results further prove the excellent gas sensing performance of FIR-120.

In theory, NO_2 can diffuse into the pores of FIR-120 because the calculated molecule size of NO_2 (0.37 nm) was smaller than the pore size of FIR-120 (0.4–0.6 nm).[61] Furthermore, the CO_2 adsorption isotherms of activated FIR-120 are also measured at ambient temperatures (Fig. S3c†) in consideration of the similar sizes of NO_2 (0.37 nm) and CO_2 (0.33 nm). The obvious CO_2 uptake of FIR-120 at room temperature further confirms this point.

To better understand the high NO_2 sensitivity of FIR-120, theoretical calculations are performed. Ti(SA)(SAH)$_2$ (H_2SA = salicylic acid) was adopted as the structure model for simplicity (Fig. S13†). The most stable model showed that oxygen from NO_2 and H from the uncoordinated –OH of the carboxylate group formed an O═N═O···H–O hydrogen bond with a length of 1.709 Å. The calculated IR spectra showed that a new peak at 1595 cm^{-1} (Fig. 4a and Movie S1†) corresponding to O–H bending vibration was attributed to the O═N═O···H–O hydrogen bond, suggesting that the free –OH groups are the main NO_2 absorption sites. *In situ* diffuse reflection infrared Fourier transform spectroscopy (DRIFTS) of FIR-120 under a NO_2 atmosphere (Fig. 4a and S13†) further proved the formation of this hydrogen bond. Two peaks at 3486 and 3024 cm^{-1} are assigned to free carboxyl –OH on FIR-120 (Fig. S13a† corresponding calculated IR spectra: 2957 cm^{-1}, Movie S2†). With the increase of NO_2 exposure time, the intensity of these peaks decreased gradually. At the same time, a new absorption peak was observed at around 1600 cm^{-1}, which was consistent with the calculated results and strongly proved the formation of the O═N═O···H–O hydrogen bond (Fig. 4a and S13b†). The intensity of these peaks gradually increased suggesting that NO_2 has a high affinity on FIR-120. Similarly, the vibration peak of the NO_2 product during the reaction was also observed, which further indicates that NO_2 interacts with FIR-120 (Table S3†).

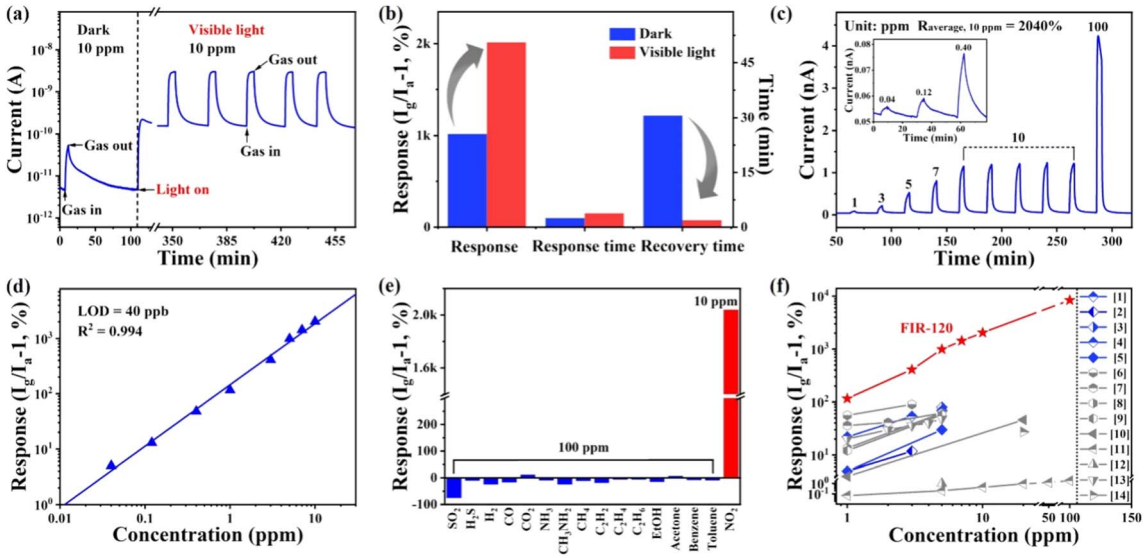

Fig. 3 (a) Response–recovery curve of FIR-120 to 10 ppm NO_2 under dark and visible light conditions. (b) Column charts of responses, response times and recovery times of FIR-120 to 10 ppm NO_2 under dark and visible light conditions. (c) Normalized response–recovery curve of FIR-120 to 10 ppm NO_2. (d) Linear log–log plot of response *vs.* concentration to NO_2 for FIR-120. (e) Selectivity of FIR-120 towards 16 interference gases. (f) Response of FIR-120 sensor as a function of NO_2 concentration and its comparison with reported MOF chemiresistor sensor materials working at room temperature: [1] $Cu_3(HHTP)_2$-thin film,[17] [2] $Cu_3(HHTP)_2$-powder,[17] [3] $Cu_3(HHTP)_2$-nanoflakes-dark,[18] [4] $Cu_3(HHTP)_2$-nanoflakes-bluelight,[18] [5] $Cu_3(HHTP)_2$-thick film,[52] [6] Pt@$Cu_3(HHTP)_2$-thin film,[17] [7] Fe_2O_3–$Cu_3(HHTP)_2$-nanoflakes,[18] [8] Pd@$Cu_3(HHTP)_2$-thick film,[52] [9] Pt@$Cu_3(HHTP)_2$-thick film,[52] [10] MIL-101(Cr)⊃PEDOT,[53] [11] ZIF-8/Au NW,[54] [12] ZIF-67 derived carbon composite-loaded MWCNTs,[55] [13] ZIF-67 derived WS_2 functionalized carbon composites,[56] and [14] SWCNT loaded PdO–Co_3O_4 derived from Pd@ZIF-67,[57] see details in Table 1.

Table 1 Gas-sensing properties toward NO_2 of various pure MOFs and MOF derivative chemiresistive sensing materials working at room temperature, as obtained in this study and reported in the literature

Material	Structure	Light source	*R*	$t_{response}$ (min)	$t_{recovery}$ (min)	Experimental LOD (ppm)	References
FIR-120	**Powder**	**Visible light**	**116% (1 ppm) 2040% (10 ppm)**	**2.48**	**2.60**	**0.04**	**This work**
Pt@$Cu_3(HHTP)_2$	Thin film	—	89.9% (3 ppm)	8.2	Non	0.1	17
$Cu_3(HHTP)_2$	Thin film	—	53.7% (3 ppm)	14	Non	0.1	
$Cu_3(HHTP)_2$	Powder	—	11.8% (3 ppm)	17.3	Non	1	
$Cu_3(HHTP)_2$	Nanoflakes	Dark	79.8% (5 ppm)	~30	Irreversible	—	58
	Nanoflakes	Bluelight	68.9% (5 ppm)	~30	Irreversible	—	
Fe_2O_3–$Cu_3(HHTP)_2$	Nanoflakes	Bluelight	~62% (5 ppm)	~30	>60	0.2	
$Cu_3(HHTP)_2$	Thick film	—	5% (1 ppm)/29.95% (5 ppm)	18	Non	—	52
Pd@$Cu_3(HHTP)_2$	Thick film	—	13.5% (1 ppm)/62.11% (5 ppm)	13.8	Non	1	
Pt@$Cu_3(HHTP)_2$	Thick film	—	12.1% (1 ppm)/57.38% (5 ppm)	14	Non	1	
MIL-101(Cr)⊃PEDOT	Pellet	—	~4% (1 ppm)/46% (20 ppm)	0.5–2.5	Irreversible	0.2	59
ZIF-8/Au NW	Thick film	—	0.9% (20 ppm)	0.12	~11.5	0.19	54
ZIF-67 derived carbon composite-loaded MWCNTs	Hybrid fibers	—	1% (5 ppm)	~3	>3	0.1	60
ZIF-67 derived WS_2 functionalized carbon composites	Pellet	—	48.2% (5 ppm)	~7	>10	0.1	56
SWCNT loaded PdO–Co_3O_4 derived from Pd@ZIF-67	Film	—	27.3% (20 ppm)	~1.5	Irreversible	10	57

Based on the above calculations and experiments, a possible sensing mechanism for FIR-120 is proposed as follows (Fig. 4b and S14†). FIR-120 shows a P-type semiconductor behavior in NO_2 sensing, which means that the hole is its main charge carrier. In the dark, NO_2 adsorbs on FIR-120 through O═N═O···H–O hydrogen bonding and captures electrons from FIR-

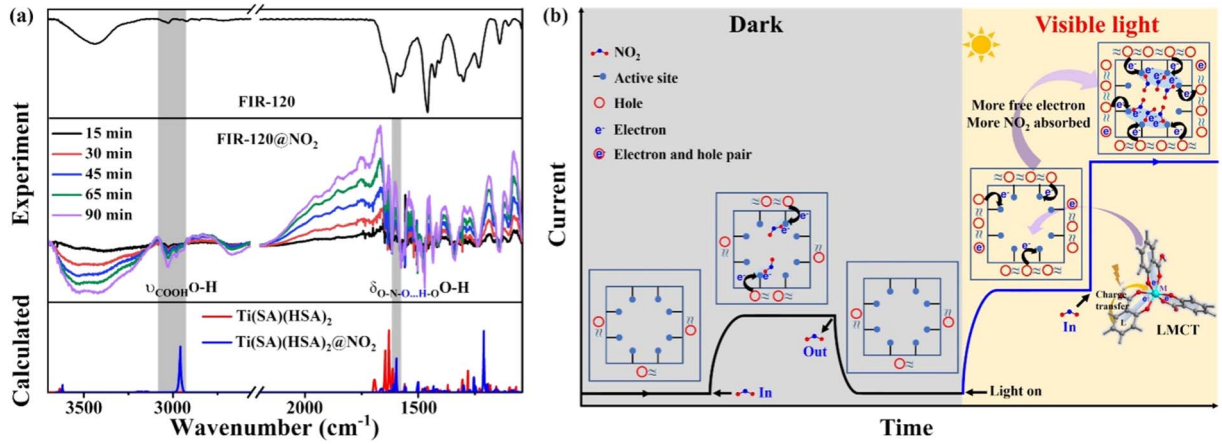

Fig. 4 (a) IR spectrum of FIR-120 (top), *in situ* diffuse reflection infrared Fourier transform spectroscopy (DRIFTS) spectra of activated FIR-120 under NO_2 (middle), and calculated IR spectra of $Ti(SA)(HSA)_2$ and $Ti(SA)(HSA)_2$ under NO_2 (bottom). (b) The proposed NO_2 gas sensing mechanism of FIR-120.

120. This process increases holes in FIR-120, corresponding to the sensing response under dark conditions. Calculations reveal that each NO_2 receives 0.217 electrons from $Ti(SA)(SAH)_2$. Meanwhile, the strong interaction between $Ti(SA)(SAH)_2$ and NO_2 ($E_{ads}(NO_2) = -0.34$ eV) makes it hard to desorb, explaining the slow recovery. Under visible light irradiation, LMCT promotes the generation and separation of electrons and hole pairs of FIR-120 to show obvious photocurrent. Calculations clearly show that the photogenerated electrons are delocalized on the structure moiety including the –OH group, which facilitates the adsorption of more NO_2 and produces more holes. Moreover, light can provide additional energy to promote molecule vibration and weakens the interaction between NO_2 and FIR-120 leading to easy desorption of NO_2, which remarkably shortens recovery time.

Conclusions

In conclusion, a visible-light active Ti-MOF with high stability and permanent porosity was rationally designed and prepared. The visible-light activity was realized by designing a LMCT functional motif through titanium-phenol bonds. The high stability and permanent porosity were achieved *via* an interpenetrating structure strategy realized using extended bridging ligands. These features endow the obtained Ti-MOF, FIR-120, with great potential as a visible-light active semiconductor. As an exemplary application, FIR-120 was used as a chemiresistive gas sensing material for trace NO_2 detection. As a result, under visible-light irradiation, it shows a response of 2040% to 10 ppm NO_2 and an experimental LOD of 40 ppb, both of which are the best among those of all reported MOFs and MOF composites at room temperature. Moreover, FIR-120 also shows excellent selectivity to NO_2 over other 15 commonly existing interfering gases. Notably, FIR-120 represents the first visible light active MOF chemiresistive sensing material, which provides guidance for the design and synthesis of high-performance visible-light active MOFs and also leads to a new type of gas sensing material.

Author contributions

Hui-Zi Li: synthesis, characterization studies of FIR-120, data curation, formal analysis, investigation, visualization, methodology and writing-original draft. Yu Pan: gas sensing, data curation, formal analysis, investigation, visualization, and methodology. Qiao-Hong Li: calculations, and result analysis. Qi-Pu Lin: structure analysis. Duo-Yu Lin: visualization. Fei Wang: conceptualization, data curation, formal analysis, investigation, writing-original draft, writing – review & editing, and funding acquisition. Gang Xu: conceptualization, formal analysis, investigation, writing – & editing, and funding acquisition. Jian Zhang: conceptualization, methodology, supervision, project administration and funding acquisition.

Conflicts of interest

There are no conflicts to declare.

Acknowledgements

This work was supported by the National Natural Science Foundation of China (21971241, 21935010, 21822109, 91961115, 21773245, and 22171263), the Natural Science Foundation of Fujian Province (2022J01505 and 2021J02017), and Fujian Science & Technology Innovation Laboratory for Optoelectronic Information of China (2021ZR101).

Notes and references

1 S.-Y. Jeong, J.-S. Kim and J.-H. Lee, *Adv. Mater.*, 2020, **32**, 2002075.
2 B. Liu, K. Li, Y. Luo, L. Gao and G. Duan, *Chem. Eng. J.*, 2021, **420**, 129881.
3 B. Wang, W. Li, Q. Lu, Y. Zhang, H. Yu, L. Huang, T. Wang, X. Liang, F. Liu, F. Liu, P. Sun and G. Lu, *ACS Appl. Mater. Interfaces*, 2021, **13**, 50121–50131.

4 Y. Cao, T. Li, Y. Gu, H. Luo, S. Wang and T. Zhang, *Small*, 2018, **14**, e1703902.
5 Y. Niu, J. Zeng, X. Liu, J. Li, Q. Wang, H. Li, N. F. Rooij, Y. Wang and G. Zhou, *Adv. Sci.*, 2021, **8**, e2100472.
6 D. Cho, J. M. Suh, S. H. Nam, S. Y. Park, M. Park, T. H. Lee, K. S. Choi, J. Lee, C. Ahn, H. W. Jang, Y. S. Shim and S. Jeon, *Adv. Sci.*, 2021, **8**, 2001883.
7 Q.-Q. Huang, Y.-Z. Li, Z. Zheng, X.-M. Jiang, S.-S. Sun, H.-J. Jiang, W.-H. Deng, G.-E. Wang, T.-Y. Zhai, M.-D. Li and G. Xu, *CCS Chem.*, 2020, **2**, 655–662.
8 Z. Meng, R. M. Stolz and K. A. Mirica, *J. Am. Chem. Soc.*, 2019, **141**, 11929–11937.
9 Y. Ren, Y. Zou, Y. Liu, X. Zhou, J. Ma, D. Zhao, G. Wei, Y. Ai, S. Xi and Y. Deng, *Nat. Mater.*, 2020, **19**, 203.
10 J. M. Suh, T. H. Eom, S. H. Cho, T. Kim and H. W. Jang, *Mater. Adv.*, 2021, **2**, 827–844.
11 T. H. Eom, S. H. Cho, J. M. Suh, T. Kim, T. H. Lee, S. E. Jun, J. W. Yang, J. Lee, S.-H. Hong and H. W. Jang, *J. Mater. Chem. A*, 2021, **9**, 11168–11178.
12 R. Gao, Z. Ying, W. Sheng and P. Zheng, *Mater. Lett.*, 2018, **229**, 210–212.
13 Y. Cheng, B. Ren, K. Xu, I. Jeerapan, H. Chen, Z. Li and J. Z. Ou, *J. Mater. Chem. C*, 2021, **9**, 3026–3051.
14 G. Cai, P. Yan, L. Zhang, H. C. Zhou and H. L. Jiang, *Chem. Rev.*, 2021, **121**, 12278–12326.
15 L. S. Xie, G. Skorupskii and M. Dinca, *Chem. Rev.*, 2020, **120**, 8536–8580.
16 M.-S. Yao, W.-H. Li and G. Xu, *Coord. Chem. Rev.*, 2021, **426**, 213479.
17 J. O. Kim, W. T. Koo, H. Kim, C. Park, T. Lee, C. A. Hutomo, S. Q. Choi, D. S. Kim, I. D. Kim and S. Park, *Nat. Commun.*, 2021, **12**, 4294.
18 Y. M. Jo, K. Lim, J. W. Yoon, Y. K. Jo, Y. K. Moon, H. W. Jang and J. H. Lee, *ACS Cent. Sci.*, 2021, **7**, 1176–1182.
19 W.-T. Koo, J.-S. Jang and I.-D. Kim, *Chem*, 2019, **5**, 1938–1963.
20 M. Zhan, S. Hussain, T. S. AlGarni, S. Shah, J. Liu, X. Zhang, A. Ahmad, M. S. Javed, G. Qiao and G. Liu, *Mater. Res. Bull.*, 2021, **136**, 111133.
21 D. M. ME, N. G. Sundaram, A. Singh, A. K. Singh and S. B. Kalidindi, *Chem. Commun.*, 2019, **55**, 349–352.
22 M. S. Yao, J. J. Zheng, A. Q. Wu, G. Xu, S. S. Nagarkar, G. Zhang, M. Tsujimoto, S. Sakaki, S. Horike, K. Otake and S. Kitagawa, *Angew. Chem., Int. Ed.*, 2020, **59**, 172–176.
23 C. Arul, K. Moulaee, N. Donato, D. Iannazzo, N. Lavanya, G. Neri and C. Sekar, *Sens. Actuators, B*, 2021, **329**, 129053.
24 Z. Meng, R. M. Stolz, L. Mendecki and K. A. Mirica, *Chem. Rev.*, 2019, **119**, 478–598.
25 M. G. Campbell, D. Sheberla, S. F. Liu, T. M. Swager and M. Dinca, *Angew. Chem., Int. Ed.*, 2015, **54**, 4349–4352.
26 M. Dan-Hardi, C. Serre, T. Frot, L. Rozes, G. Maurin, C. Sanchez and G. Ferey, *J. Am. Chem. Soc.*, 2009, **131**, 10857–10859.
27 S. Yuan, T.-F. Liu, D. Feng, J. Tian, K. Wang, J. Qin, Q. Zhang, Y.-P. Chen, M. Bosch, L. Zou, S. Teat, S. Dalgarno and H.-C. Zhou, *Chem. Sci.*, 2015, **6**, 3926–3930.
28 Y. Fu, D. Sun, Y. Chen, R. Huang, Z. Ding, X. Fu and Z. Li, *Angew. Chem., Int. Ed.*, 2012, **51**, 3364–3367.
29 H. L. Nguyen, F. Gandara, H. Furukawa, T. L. H. Doan, K. E. Cordova and O. M. Yaghi, *J. Am. Chem. Soc.*, 2016, **138**, 4330–4333.
30 Y. Keum, S. Park, Y. P. Chen and J. Park, *Angew. Chem., Int. Ed.*, 2018, **57**, 14852–14856.
31 H. Li, Y. Sun, Z. Y. Yuan, Y. P. Zhu and T. Y. Ma, *Angew. Chem., Int. Ed.*, 2018, **57**, 3222–3227.
32 S. Wang, T. Kitao, N. Guillou, M. Wahiduzzaman, C. Martineau-Corcos, F. Nouar, A. Tissot, L. Binet, N. Ramsahye, S. Devautour-Vinot, S. Kitagawa, S. Seki, Y. Tsutsui, V. Briois, N. Steunou, G. Maurin, T. Uemura and C. Serre, *Nat. Commun.*, 2018, **9**, 1660.
33 C. Li, H. Xu, J. Gao, W. Du, L. Shangguan, X. Zhang, R.-B. Lin, H. Wu, W. Zhou, X. Liu, J. Yao and B. Chen, *J. Mater. Chem. A*, 2019, **7**, 11928–11933.
34 S. Smolders, T. Willhammar, A. Krajnc, K. Sentosun, M. T. Wharmby, K. A. Lomachenko, S. Bals, G. Mali, M. B. J. Roeffaers, D. E. De Vos and B. Bueken, *Angew. Chem., Int. Ed.*, 2019, **58**, 9160–9165.
35 X. Wang, X. Zhang, W. Zhou, L. Liu, J. Ye and D. Wang, *Nano Energy*, 2019, **62**, 250–258.
36 A. Cadiau, N. Kolobov, S. Srinivasan, M. G. Goesten, H. Haspel, A. V. Bavykina, M. R. Tchalala, P. Maity, A. Goryachev, A. S. Poryvaev, M. Eddaoudi, M. V. Fedin, O. F. Mohammed and J. Gascon, *Angew. Chem., Int. Ed.*, 2020, **59**, 13468–13472.
37 Y. Sun, D.-F. Lu, Y. Sun, M.-Y. Gao, N. Zheng, C. Gu, F. Wang and J. Zhang, *ACS Mater. Lett.*, 2021, **3**, 64–68.
38 L. Zhang, F. F. Li, J. J. You, N. B. Hua, Q. T. Wang, J. H. Si, W. Z. Chen, W. J. Wang, X. Y. Wu, W. B. Yang, D. Q. Yuan, C. Z. Lu, Y. R. Liu, A. M. Al-Enizi, A. Nafady and S. Q. Ma, *Chem. Sci.*, 2021, **12**, 5767–5773.
39 J. Zhu, P.-Z. Li, W. Guo, Y. Zhao and R. Zou, *Coord. Chem. Rev.*, 2018, **359**, 80–101.
40 J. Gao, J. Miao, P. Z. Li, W. Y. Teng, L. Yang, Y. Zhao, B. Liu and Q. Zhang, *Chem. Commun.*, 2014, **50**, 3786–3788.
41 N. T. T. Nguyen, H. Furukawa, F. Gandara, C. A. Trickett, H. M. Jeong, K. E. Cordova and O. M. Yaghi, *J. Am. Chem. Soc.*, 2015, **137**, 15394–15397.
42 H. Assi, L. C. Pardo Perez, G. Mouchaham, F. Ragon, M. Nasalevich, N. Guillou, C. Martineau, H. Chevreau, F. Kapteijn, J. Gascon, P. Fertey, E. Elkaim, C. Serre and T. Devic, *Inorg. Chem.*, 2016, **55**, 7192–7199.
43 N. M. Padial, J. Castells-Gil, N. Almora-Barrios, M. Romero-Angel, I. da Silva, M. Barawi, A. Garcia-Sanchez, V. A. de la Pena O'Shea and C. Marti-Gastaldo, *J. Am. Chem. Soc.*, 2019, **141**, 13124–13133.
44 J. Cao, W. Ma, K. Lyu, L. Zhuang, H. Cong and H. Deng, *Chem. Sci.*, 2020, **11**, 3978–3985.
45 S.-P. Guo, Y. Chi and G.-C. Guo, *Coord. Chem. Rev.*, 2017, **335**, 44–57.
46 G. C. Guo, Y. G. Yao, K. C. Wu, L. Wu and J. S. Huang, *Prog. Chem.*, 2001, **13**, 151–153.
47 D. Zhao, D. J. Timmons, D. Yuan and H.-C. Zhou, *Acc. Chem. Res.*, 2011, **44**, 123–133.

48 M.-Y. Gao, K. Wang, Y. Sun, D. Li, B.-Q. Song, Y. H. Andaloussi, M. J. Zaworotko, J. Zhang and L. Zhang, *J. Am. Chem. Soc.*, 2020, **142**, 12784–12790.
49 V. A. Blatov, A. P. Shevchenko and D. M. Proserpio, *Cryst. Growth Des.*, 2014, **14**, 3576–3586.
50 L. Sarkisov and A. Harrison, *Mol. Simul.*, 2011, **37**, 1248–1257.
51 A. L. Spek, *Acta Crystallogr., Sect. C: Struct. Chem.*, 2015, **71**, 9–18.
52 W. T. Koo, S. J. Kim, J. S. Jang, D. H. Kim and I. D. Kim, *Adv. Sci.*, 2019, **6**, 1900250.
53 B. Le Ouay, M. Boudot, T. Kitao, T. Yanagida, S. Kitagawa and T. Uemura, *J. Am. Chem. Soc.*, 2016, **138**, 10088–10091.
54 P. Li, H. Zhan, S. Tian, J. Wang, X. Wang, Z. Zhu, J. Dai, Y. Dai, Z. Wang, C. Zhang, X. Huang and W. Huang, *ACS Appl. Mater. Interfaces*, 2019, **11**, 13624–13631.
55 K. Rui, X. Wang, M. Du, Y. Zhang, Q. Wang, Z. Ma, Q. Zhang, D. Li, X. Huang, G. Sun, J. Zhu and W. Huang, *ACS Appl. Mater. Interfaces*, 2018, **10**, 2837–2842.
56 W.-T. Koo, J.-H. Cha, J.-W. Jung, S.-J. Choi, J.-S. Jang, D.-H. Kim and I.-D. Kim, *Adv. Funct. Mater.*, 2018, **28**, 1802575.
57 S. J. Choi, H. J. Choi, W. T. Koo, D. Huh, H. Lee and I. D. Kim, *ACS Appl. Mater. Interfaces*, 2017, **9**, 40593–40603.
58 Y. M. Jo, K. Lim, J. W. Yoon, Y. K. Jo, Y. K. Moon, H. W. Jang and J. H. Lee, *ACS Cent. Sci.*, 2021, **7**, 1176–1182.
59 B. Le Ouay, M. Boudot, T. Kitao, T. Yanagida, S. Kitagawa and T. Uemura, *J. Am. Chem. Soc.*, 2016, **138**, 10088–10091.
60 K. Rui, X. Wang, M. Du, Y. Zhang, Q. Wang, Z. Ma, Q. Zhang, D. Li, X. Huang, G. Sun, J. Zhu and W. Huang, *ACS Appl. Mater. Interfaces*, 2018, **10**, 2837–2842.
61 B. Delley, *J. Chem. Phys.*, 2000, **113**, 7756–7764.